Using x-ray reflectivity to determine the structure of surfactant monolayers

B. B. Luokkala,[1,2] S. Garoff,[1,2] and R. M. Suter[1]
[1]*Department of Physics, Carnegie Mellon University, Pittsburgh, Pennsylvania 15213*
[2]*Colloids, Polymers, and Surfaces Program, Carnegie Mellon University, Pittsburgh, Pennsylvania 15213*
(Received 11 February 2000)

Interactions among the multiple degrees of freedom of surfactant molecules cause fascinating richness in the structure of their monolayers. Beyond this scientific motivation for studying surfactant monolayers, the technological use of monolayers for interfacial control and molecular assembly demands a clear understanding of monolayer structure. X-ray and neutron reflectivity have become prime techniques for determining this structure. We present x-ray reflectivity data for a representative surfactant monolayer system and outline an objective procedure for obtaining the maximum amount of structural information possible. Our approach combines tight control of instrumental parameters, dynamically optimized Monte Carlo and simulated annealing to probe the χ^2 hypersurface, and a set of statistical criteria for accepting and rejecting fits. We justify our procedure through tests using simulated data. Results indicate that an ensemble of fits must be performed for each set of reflectivity data in order to survey the χ^2 hypersurface adequately. A single good fit may yield structural parameters which are quite misleading, yet physically plausible. Thus, one must never be satisfied with performing just a single fit. In cases for which multiple, statistically equivalent fits are obtained, the apparent ambiguity is substantially mitigated by averaging the parameters over the ensemble of good fits. We also introduce a method of dealing with cases for which a good fit may be extremely difficult to find. Our analysis procedures can be generalized to other monolayer or multilayer systems and are also applicable to neutron reflectivity.

PACS number(s): 68.45.−v, 61.10.Kw, 68.55.−a

I. INTRODUCTION

The multiple internal degrees of freedom and the amphiphilic character of surfactant molecules lead to rich and subtle structural variation in assemblies of these molecules [1]. The tendency of surfactants to assemble at interfaces leads to their use in a wide variety of technologies, including complex fluid formulation; interfacial control for wetting, adhesion or lubrication; and molecular assembly for device applications [2]. Thus both fundamental and applied objectives require accurate, reliable determination of the structure of surfactant assemblies. In the characterization of monolayer assemblies, x-ray and neutron reflectivity play a prime role, along with diffraction, vibrational spectroscopies, and imaging scanning probe techniques. The purpose of the present work is to outline a procedure for measuring and interpreting x-ray reflectivity data which maximizes the structural information obtained from a surfactant monolayer at the solid/vapor interface. The technique for data interpretation is applicable not only to surfactants but to any monolayer structure and to neutron reflectivity as well.

The amphiphilic property of surfactant molecules gives rise to self-assembled structures at interfaces as well as in bulk. The structure of these assemblies depends upon the nature of the individual molecules and surfactant concentration. If the solvent is polar, the hydrophobic/hydrophilic interaction tends to minimize contact between the solvent and the nonpolar hydrocarbon tail groups and to maximize contact between the solvent and the polar head groups. Thus, micelles, vesicles, or other partially ordered phases form. The size and shape of these structures depend upon the electrostatic and steric repulsion of the head groups in competition with the van der Waals attraction of the tail groups. In addition to these intermolecular forces, intramolecular forces affect the average volume occupied by the tail groups. While *trans* isomerization is energetically favored in a hydrocarbon chain, the presence of some *gauche* bonds may be entropically stabilized.

Structures formed at solid/liquid and liquid/vapor interfaces are likely to be different from those in bulk solution due to the additional interaction between the surfactant molecules and the solid surface and the constraints of the two-dimensional interface. All of the interactions mentioned above dictate the area occupied by each molecule at an interface. They also determine how volume is filled when other constraints dictate molecular spacing (e.g., assembling on an ordered surface, surface pressure in Langmuir-Blodgett deposition, etc.) or when the molecular structure itself provides multiple length scales [3]. A monolayer may be deposited at the solid/vapor interface either by self-assembly at the solid/liquid interface during immersion or by the Langmuir-Blodgett technique as the solid is withdrawn from solution. In either case, the solid substrate is drawn out of solution through a bulk meniscus and the molecular monolayer produced at the solid/vapor interface may not have sufficient mobility to access equilibrium configurations.

There are several important aspects to monolayer structure. The overall thickness of the surfactant monolayer provides information about the average tilt of the molecules and the extent to which the tail groups exist in the all *trans* configuration. The packing density describes the free volume afforded each molecule. Thus, through systematic studies of homologous series, we may gain insight into the mechanism controlling the molecular spacing. The density of counterions present in the head group region of an ionic surfactant monolayer reveals the nature of the surfactant/surface bind-

ing mechanism. The roughness of the interfaces bounding the monolayer provides further information on disorder in the monolayer.

We attempt to maximize the accuracy and precision of our reflectivity technique with the goal of evaluating the efficacy of the method to determine the underlying causes of monolayer structure. We compare parameters and their uncertainties to benchmark values of quantities known to characterize the physics controlling structure in a variety of monolayer or layered surfactant assemblies. First, the electron density in the hydrocarbon tail region should not exceed 6.0×10^{23} e/cm^3, corresponding to close-packed alkane chains. In the liquidlike lamellar phase of lipids, L_α, the electron density is approximately 15% less than this but values considerably lower may occur even for a complete monolayer if the spacing is dominated by the size of the head group. Second, the area per molecule of our monolayers can be compared to the area per hydrocarbon chain of (a) crystalline hydrocarbons, where the hydrocarbon tails are all *trans* and tightly packed (19 Å^2) [4]; (b) the hydrocarbon tails of the L_β lamellar phase of a typical lipid, where the chains are mainly *trans* and packed in a less well ordered array (24 Å^2) [5]; and (c) the hydrocarbon tails of the L_α lamellar phase of a typical lipid, where the chains are almost liquidlike with many *gauche* bonds (31 Å^2) [6]. Third, the uncertainty in the determination of monolayer thickness can be compared to the 15% reduction in thickness due to chain disordering in the transition from the L_β to L_α phase of DLPE [7] or a similar size change due to a typical chain tilt in a monolayer consisting of ordered chains [8]. Fourth, the precision of the determination of the electron density of a head group region can be compared to the possible difference in density due to counterions in an ionic monolayer, e.g., the electron density of the head group region in a monolayer of sodium dodecyl sulfate (SDS) increases by 25% if all of the Na^+ counterions are present compared to the density if no counterions are present. Finally, roughnesses of the interfaces of the monolayer should be compared to the typical rms roughness of our oxide surfaces (2–4 Å), thus revealing if the monolayer smooths over substrate roughness.

All of the desired structural details can, in principle, be determined by means of x-ray reflectivity which probes electron density gradients normal to a surface [9–14]. However, the rapid falloff of specular intensity with angle of incidence and the presence of diffuse scattering limit the accessible range of momentum transfer. This in turn sets a lower limit on the length scale of structural features which can be probed. A complementary technique, neutron reflectivity, uses isotopic substitution to enhance contrast between layers [14,16]. However, the same limitations on discernible length scales apply to an even greater degree, since the intensity of neutron sources is generally much less than the sources for x-ray reflectivity. Finally and perhaps most important, the nonlinearity of the functions to be fit to reflectivity data insures that the χ^2 hypersurface will be highly convolved with the likelihood of multiple local minima.

Various approaches to analysis and interpretation of reflectivity data have been proposed [17–19]. Of particular note is the implementation of genetic algorithms as an efficient method of finding the best possible fit [19]. If the χ^2 hypersurface contains a single global minimum which is sufficiently sharp and difficult to locate, as is the case for high signal-to-noise data, genetic algorithms may have an advantage over other search techniques. However, as some authors have discussed, there are situations in which the fit is not unique, and the interpretation is rendered ambiguous [18,20,21]. We propose a method of analysis which mitigates the problem of nonuniqueness of fits and enables a good fit to be found even for high signal-to-noise data.

In this paper we show that obtaining justified conclusions concerning monolayer structure demands focus on four issues: (a) careful measurement of all instrumental parameters, (b) judicious choice of the number of fitting parameters, (c) careful attention to the statistics which indicate a ''good'' fit and statistically equivalently ''good'' fits, and (d) thorough surveying of the χ^2 hypersurface to sample the ensemble of fits describing the data. In the next section we describe both our experimental techniques, emphasizing careful measurement of instrument parameters, and our analysis techniques, stressing the nature of the χ^2 hypersurface and the criteria for statistical equivalence of different fits. In Sec. III we illustrate the problems of ambiguity of interpretation with examples of experimental data and simulated data. The experimental data are from a monolayer of SDS. We show how a cursory analysis suggests that the structure of the monolayer cannot be determined unambiguously from the fits. We then generate and analyze simulated data for monolayers of SDS in order to determine whether the ambiguity is an instrumental artifact or intrinsic to the experiment. Results of the simulations suggest that the ambiguity arises from insufficient surveys of the χ^2 hypersurface and improper interpretation of the meaning of a hypersurface with multiple, statistically equivalent local minima. The apparent ambiguity in monolayer structure is substantially removed by averaging parameters over an ensemble of statistically equivalent fits. We then return to the experimental data, performing a more thorough search of the χ^2 hypersurface to find as many good fits as possible. The average of parameters over this ensemble of fits yields a model which is physically plausible and has very little structural ambiguity. In Sec. IV, we discuss the effects of increased signal-to-noise ratio, which might be attained using synchrotron sources. With better counting statistics, the correct structural model can be recovered from the data with a higher degree of accuracy. However, a good fit to the data may become more difficult to find. We conclude in Sec. V with a brief discussion of simulations for other monolayer structures and a general statement of a protocol for data collection and analysis.

II. EXPERIMENTAL AND ANALYSIS TECHNIQUES

A. Measurement procedure

Our apparatus has been described previously [9,10]. Here, we emphasize points important for measuring accurate, absolute reflectivity curves. The momentum transfer normal to the substrate surface is $Q=2k\sin\alpha$, with k being the x-ray wave number and α the grazing angle of incidence. The observed reflectivity signal, $R(Q)$, is affected by a number of instrumental factors [13]. We take considerable care in setting up measurements so that these factors are well determined. We use a rotating anode source with a fine focus filament, operated at a maximum of 5.2 kW. A vertically

bent graphite monochromator selects copper K_α radiation. The incident beam shape and divergence are controlled by two sets of XY slits located 100 mm and 454 mm upstream from the sample position. The vertical focusing yields a beam height (parallel to the surface) at the sample of 3 mm. Because of this vertical focusing, the reciprocal space resolution in the out-of-plane direction is quite broad. In the horizontal direction, we typically use a beam width of 0.2 mm as defined by the slits closest to the sample. The upstream slits and the x-ray source size determine the angular divergence in the scattering plane. This divergence determines the resolution width of the measurement in the radial direction along the specular ridge. Because of the small source size, it is not trivial to calculate this divergence so we determine it from rocking scans through the (111) Bragg peak of the silicon substrate.

A linear position-sensitive detector (PSD) measures the specular and nearby diffuse scattering at each angle of incidence [9]. The PSD has the advantage over standard techniques of explicitly displaying the specular scattering and the diffuse background. The data reduction program fits a five-parameter PSD response function (a Gaussian with weak Lorentzian tails [9]) plus a linear background to each PSD data set. Since the program generates a full set of plots of the PSD scans and associated fitting parameters, spurious backgrounds and any alignment errors which could affect the data are evident. The separation of the signal at high Q into specular and diffuse components depends on the instrumental resolution. In our experiments the typical angular width of the specular peak is 0.02°. Diffuse scattering from the sample prevents measurement of signals weaker than $R(Q) \sim 10^{-8}$. That is, at large Q, the PSD data sets contain no specular peak but have a background well above either the detector dark counts per channel (typically less than 2×10^{-4} per second) or the background present with the beam on but no sample present. Since the apparent intensity of diffuse scattering is resolution-dependent, the use of a synchrotron source can improve the signal-to-noise ratio and may extend the range of momentum transfer. But as we shall show, this may render a good fit to the data extremely difficult to find.

To cover many decades of reflectivity, we adjust x-ray generator power, absorbers, and counting time. For a given set of these instrumental quantities, we collect data over some range of α. At small angles where counting times are short, we collect overlapping data sets so that the reduction program can normalize the sets to each other by matching. The first data set is normalized to the incident intensity determined by a direct measurement of the beam made before the sample is put in place. At large α where counting times are long, we normalize the data using an incident beam monitor so that slow fluctuations in source strength do not distort the data.

Sample alignment requires the definition of the $\alpha=0$ condition and the placement of the sample surface on the α rotation axis. Sample positioning is achieved by a set of ''beam block'' scans in which the detector is positioned to receive the incident beam (with a narrow receiving slit that blocks any reflected beam). Then α is varied to block the beam with first one and then the other end of the substrate. The sample is translated into the beam until the peak intensity in the beam block scan is one-half that of the incident beam. α is set to zero at the position of this peak intensity. If the rotation axis passes through the middle of the in-plane length of the sample, then the beam block is symmetric about $\alpha=0$. The final beam block scan also shows the angle α_b at which the entire incident beam falls on the sample. Within errors due to the beam profile, the observed angle should be $\alpha_b = w/L$, where w is the beam width and L is the length of the sample [13].

B. Samples

Our substrates are polished silicon (111) crystals with the native oxide layer on the surface. The crystals are 50 mm×40 mm×3 mm and are supplied by Semiconductor Processing Company, Boston MA. Crystals of this thickness are preferred over thinner silicon wafers, which are more likely to be macroscopically bowed. Bowing reduces the effective resolution and thereby reduces the ratio of specular to diffuse scattering. Substrates are cleaned by a standard chemical process that produces a charged surface under pH7 water [15,22]. Surfactant monolayers are produced by dipping the crystal in solutions with surfactant concentrations below 0.5 times the critical micellar concentration [15,16]. Reflectivity curves for samples discussed in this paper were measured in air. Repeated measurements are performed to verify that the low-energy surface of the monolayer has not become contaminated and is not significantly damaged by x-ray radiation.

C. Theory and data fitting

While our fitting uses the more rigorous optical matrix method [23], the Born approximation is helpful for qualitatively relating the scattering in reciprocal space to real space density variations. In this approximation, the specular reflectivity is given by the Fourier transform of the gradient of the laterally averaged electron density [13,24]:

$$R(Q) = \frac{A}{Q^4}\left\langle \left| \int dz \frac{d\overline{\rho}}{dz} e^{iQz} \right|^2 \right\rangle, \tag{1}$$

where A is a constant, $\langle \cdots \rangle$ denotes an ensemble average, and

$$\overline{\rho}(z) = \frac{1}{L_x L_y} \int_{L_x} dx \int_{L_y} dy \rho(x,y,z). \tag{2}$$

L_x and L_y are coherence lengths determined by experimental parameters and ρ is the local electron density. The coherence length out of the scattering plane, L_y, is very small due to the broad resolution in this direction. The in-plane averaging length, L_x, is of the order of ten microns. Measurement at Q probes variations in $\overline{\rho}$ or $d\overline{\rho}/dz$ of length $\lambda = 2\pi/Q$. Roughly speaking, to resolve structure down to $\lambda_{\min}$ requires measurement to $Q_{\max} = 2\pi/\lambda_{\min}$. Interference fringes in the reflectivity data suggest layers of relatively constant $\overline{\rho}$ bounded by relatively abrupt changes in $\overline{\rho}$.

In our analysis, we parametrize electron density variations as shown in Fig. 1. The quantity of basic importance is the index of refraction, $n = 1 - \delta + i\beta$, where δ and β are pro-

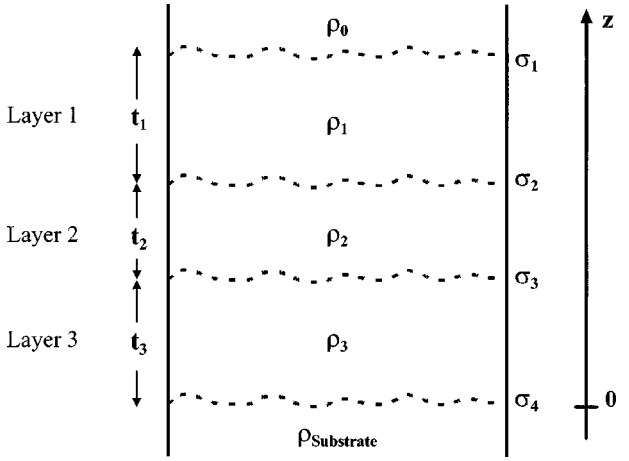

FIG. 1. A schematic diagram showing the parametrization of a surfactant layer on a silicon substrate. ρ_i and t_i are densities and thicknesses for each layer, while σ_i are effective interface widths or roughnesses. The z axis is perpendicular to the film plane and we define the zero at the nominal position of the bulk silicon surface. Air is above layer 1 and bulk silicon is below layer 3.

portional to the local electron density. We write $\delta = (\lambda^2/2\pi)\rho b$, where ρ is the molecular number density of molecules having scattering length

$$b = r_e \sum_i Z_i^{\mathrm{eff}} N_i . \tag{3}$$

r_e is the classical electron radius, Z_i^{eff} the effective number of electrons on atom type i (including anomalous effects), and N_i the number of such atoms in the molecule. Similarly, $\beta = (\lambda/4\pi)\rho s$, with

$$s = \sum_i \mu_i M_i N_i , \tag{4}$$

where μ_i is the absorption coefficient for atom type i and M_i is the atomic mass. As described in the Appendix, we can fit to δ and/or β separately or couple the variations in δ and β via the chemical formula unit number density within the layer. The latter is practical, for example, when the stoichiometry of a layer is known or when it is reasonable to partition the surfactant layer into sublayers containing the head and the tail only, with no intermixing of these units across the layer boundary. The former method is required if we do not want to bias our interpretation by the rather unrealistic assumption of no intermixing of head and tail across the relatively abrupt variation of the electron density. Absorption is a small effect for thin layers, primarily affecting reflectivity near the critical angle. In the present work, we vary δ for the surfactant and for the native SiO_2 layer, but keep it fixed at the known value for the silicon substrate. The value of β is two orders of magnitude smaller than δ for most materials. In this work, we keep each β fixed at a nominal value appropriate to the material (hydrocarbon, SiO_2 or Si). This assumption does not affect the results reported here.

Also indicated in Fig. 1 are the interface widths, σ_i, which characterize the smooth but relatively abrupt transition in electron density across an interface. We assume these transitions have error function forms. The use of a smooth transition is justified by the fact that the measurement reports *laterally averaged densities* within the coherence length of the x rays and *ensemble averaged intensities* across the beam width as emphasized in Eqs. (1) and (2). The local electron density may vary smoothly across an interface due to a smooth evolution in molecular concentration variables. An additional width is generated by the fact that the interface itself may vary in position due to static roughness [24] (or on a fluid surface, kinetic undulations) within the length scale L_x. It should be emphasized that if roughnesses have an amplitude comparable to or larger than the thickness of a bounding layer, then that layer is effectively removed from the scattering signal.

Our computer program, SPEEDO, uses a combination of dynamically optimized Monte Carlo [25,26] and simulated annealing [27] techniques to attempt to find the global minimum of the χ^2 hypersurface. The program models instrumental effects and offers a variety of options as described in the Appendix. In work on surfactant monolayers, one should compute the model reflectivity with the rigorous matrix method [23,28] rather than the Nevot-Croce approximation [29] because layer thicknesses are likely to be comparable to bounding roughnesses. The program is initialized by specifying starting points and reasonable limits for each of the fitting parameters. To illustrate what we mean by reasonable limits, a surfactant monolayer layer thickness may be allowed to vary between zero and twice the fully extended molecule length, so as not to rule out the possibility of a bilayer, and the electron density of the hydrocarbon tail group may not exceed that of crystalline hydrocarbon chains. In the fits presented here, only those parameters which describe the layer structure are varied. Other parameters which take into account the geometry of the sample and the instrumental resolution are determined independently in the laboratory and are kept fixed. A typical fit for a surfactant layer on a silicon crystal with a native oxide layer involves ten floating parameters: four roughnesses, three thicknesses, and three densities. The electron density of bulk silicon is fixed to its known value.

In order to define the language used below, we need to review the statistics of least-squares fitting. χ^2, the function being minimized in the fit, is defined according to the expression

$$\chi^2 = \sum_{i=1}^{N} \left[\frac{r(Q_i) - f(Q_i, \{p\})}{e_i} \right]^2 , \tag{5}$$

where the $r(Q_i)$ are the measured reflectivity data with uncertainties, e_i, assigned according to Poisson statistics. The $f(Q_i, \{p\})$ are the calculated reflectivities for a particular set of model parameters, $\{p\}$. The assumption of Poisson statistics for our measured intensities is justified since we do not operate near the dark count levels of our detector. The ''standard errors'' in the fitting parameters are set by the $\chi^2_{\min} + 1$ contour about the minimum in the χ^2 hypersurface [30].

If several sets of data are obtained from the same physical system, the value of χ^2 for a fixed set of fitting parameters will vary from one data set to another due to Poisson noise on the data. There exists an average value of χ^2 for the ensemble of data sets and a standard deviation about this mean. For a set of model parameters which represents an

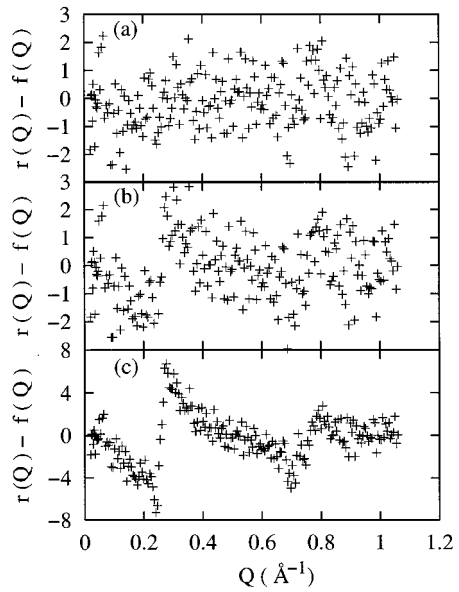

FIG. 2. Examples of residuals plots for (a) a good fit, (b) a marginally unacceptable fit, whose χ^2 exceeds the best fit χ^2 by more than $2e_{\chi^2}$, and (c) a poor fit with obvious systematic deviations.

adequate characterization of the measurement, the mean value of χ^2 is $\nu=N-d$, where N is the number of data points, d is the number of fitting parameters, and ν is the number of degrees of freedom in the fit [31]. The ''uncertainty'' in χ^2 is calculated by taking partial derivatives of Eq. (5) with respect to the $r(Q_i)$, multiplying by e_i, and adding terms in quadrature. The result is

$$e_{\chi^2}=2\sqrt{\nu}. \tag{6}$$

The reduced chi-square, χ^2_ν, is defined as χ^2/ν and should have unit mean and a standard deviation, $e_{\chi^2_\nu}=2/\sqrt{\nu}$. Any sets of parameters which yield χ^2 values within e_{χ^2} of the lowest χ^2 are *statistically indistinguishable*. If, for one data set, $\{p\}_0$ is the optimal parameter set with χ^2_0, a different data set from the same physical system will likely yield, for $\{p\}_0$, a χ^2 value within e_{χ^2} of χ^2_0, but a different parameter set, $\{p\}_1$, will be optimal. We cannot select between $\{p\}_0$ and $\{p\}_1$ as being more likely to correctly describe the monolayer.

We also include in our analysis plots of the residuals,

$$\Delta_i=\frac{r(Q_i)-f(Q_i,\{p\})}{e_i}. \tag{7}$$

Ideally, 95% of the residuals should fall within a band about zero of width ± 2. Most important, the fluctuations should have no near-neighbor correlations. An example of such a residuals plot is shown in Fig. 2(a). We use the residuals plot to look for ''systematic deviations,'' defined as any oscillation having a ''wavelength'' which is an appreciable fraction of the momentum transfer range covered by the entire data set. Examples of residuals plots showing systematic deviations are shown in Figs. 2(b) and 2(c).

Thus, we arrive at two criteria for statistical acceptance of a set of parameters. The first criterion is to demand that the residuals plot show no systematic features. In addition, we demand that the χ^2 value be within e_{χ^2} of the best value we find. Fits which satisfy these criteria are termed ''good'' fits. Multiple fits fulfilling these criteria must be considered equally valid in determining monolayer structure.

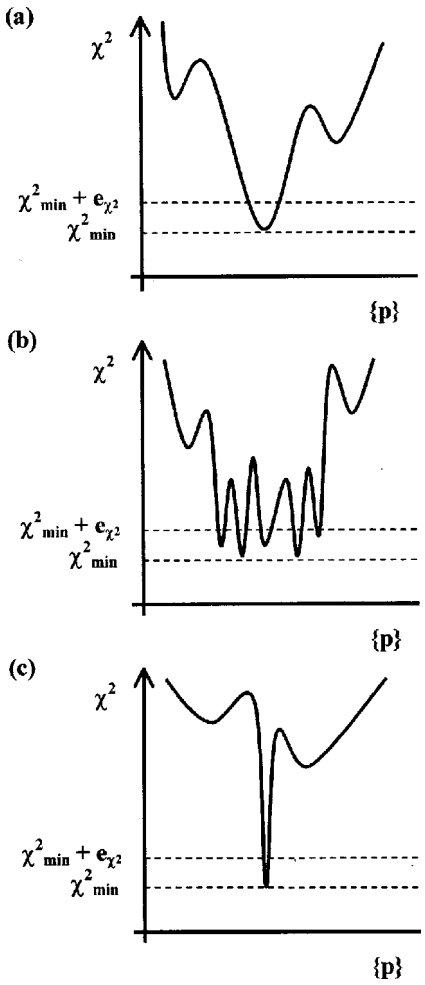

FIG. 3. Illustrations of possible structure of the χ^2 hypersurface. (a) The ideal situation: a single global minimum corresponding to a good fit, local minima corresponding to poor fits; (b) multiple, statistically equivalent minima, all corresponding to good fits: a thorough survey of the hypersurface must be performed to avoid ambiguity or misleading results; and (c) the single minimum for high signal-to-noise data may be extremely narrow and difficult to locate by a random search process.

For a fit with d free parameters, the χ^2 function is a $(d+1)$-dimensional hypersurface. A two-dimensional cut through the hypersurface is illustrated schematically in Fig. 3. In an ideal situation, the best fit corresponds to a single global minimum on the hypersurface [Fig. 3(a)]. Any other local minima should correspond to fits which are unacceptable by the criteria set forth above. In practice, there are situations in which the hypersurface contains one or more minima which are statistically indistinguishable from the global minimum and show no systematic residuals, but are sufficiently separated in parameter space to cause ambiguity in the physical description of the monolayer [Fig. 3(b)]. We discuss two examples in detail in Sec. III.

Our general strategy for analysis is to initialize the simulated annealing program from several different parameter

sets and to run the program multiple times from each set of initial conditions. These initial conditions are widely separated in parameter space, as evidenced by the variation in the initial value of χ^2, but all are within physically plausible limits. This enables us to probe the χ^2 hypersurface and to locate as many good fits to the data as possible. We calculate the average and standard deviation of the values of each parameter across all the good fits. As more good fits are found, the uncertainty (standard deviation) of the ensemble averaged parameters is reduced. When the parameter uncertainties have been reduced to the point at which we can draw conclusions about the structure with reasonable confidence, we call an end to the fitting process.

A given attempt to fit data from a specific set of initial values of the parameters results in one of three possible outcomes. (a) The desirable outcome is a ''good'' fit as judged by the residuals plot, χ^2 value, and the fact that none of the parameters has saturated at the preset limits. In this paper, we rely only on fits this type. (b) One or more of the parameters saturates at the preset limits. If this occurs we do not count the fit as legitimate, regardless of the quality of the fit. (c) The fit yields a parameter set that is within preset limits but the fit is not ''good,'' as indicated by a residuals plot with systematic deviations. This may occur if the model is insufficient to describe the data or if the fit locates and does not escape from a local minimum in the χ^2 hypersurface. If a large number of attempts fails to find a good fit, we conclude that the model must be insufficient. The model is then made more general by subdividing a layer into two parts. If high counting statistics are attained on all data points, an acceptable fit may exist but the minimum in the χ^2 hypersurface may be very narrow and hard to find [see Fig. 3(c)]. We discuss methods of dealing with this case in Sec. IV.

III. STATISTICAL DETERMINATION OF MONOLAYER STRUCTURE

A. Analysis of experimental data from an SDS layer

In this section we present the results of fits to experimental data obtained from an SDS monolayer on silicon. This exercise demonstrates the problems described above. The data, shown in Fig. 4, span more than eight decades in reflectivity and extend to $Q_{\max}=0.74$ Å^{-1} or $\lambda_{\min}\approx 9$ Å. As discussed in Sec. II, all instrumental parameters were as carefully determined as possible. Attempts to fit the data to a model with two layers (surfactant plus oxide) yield statistically unsatisfactory results so we fit the data to a model with three layers: two regions representing the SDS monolayer and one representing the silicon oxide. We recognize that adding a layer to the model adds three parameters to the fit, and thus may overparametrize the data. This may lead to the multiplicity of good fits we find. However, imposing a constraint coupling the properties of the surfactant sublayers would require precise knowledge of some aspect of film structure. In the present case, we have no such knowledge.

To obtain a reasonably complete survey of the χ^2 hypersurface, we start the simulated annealing from three widely different initial parameter sets. In this exercise, a total of thirteen simulated annealings were performed. This revealed three ''good'' fits with statistically equivalent χ^2. Each of the good fits was obtained from more than one of the initial

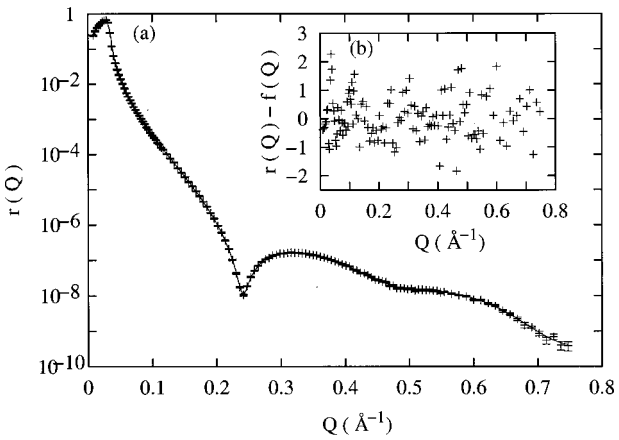

FIG. 4. Experimental data from an SDS layer on a silicon substrate. The solid line is one of three statistically equivalent good fits. The inset shows a plot of the residuals as defined in Eq. (7). Parameters for the three fits are shown in Table I.

parameter sets. The results of these fits are shown in Table I. However, the parameter sets from these fits are statistically distinct, i.e., the parameters do not agree within the standard errors. The solid line in Fig. 4 is one of the three acceptable fits. The inset shows no systematic variations in the residuals; virtually all deviations are less than two error bars. Figure 5 shows $\delta(z)$ for the three fits. Clearly, different density profiles describe the same data equally well.

In fact, these acceptable fits suggest very different physics governing the SDS monolayer structure. In fit *C*, the electron

TABLE I. Three fits to experimental data from an SDS monolayer. Fitting parameters are as defined in Fig. 1. Quantities in italics are derived from the fitting parameters. Numbers in parentheses indicate the uncertainty in the preceding digit. The column labeled ''average'' is the (unweighted) mean and standard deviation of 21 good fits to the data. The value of $\delta_{\mathrm{Si}}=7.37\times10^{-6}$ was fixed to correspond to the bulk density.

Parameter	Fit *A*	Fit *B*	Fit *C*	21 fit average
σ_1 (Å)	2.163(6)	2.390(6)	2.479(1)	2.4(1)
t_1 (Å)	15.52(1)	10.77(1)	11.820(5)	10.5(8)
$10^6\delta_1$	1.79(1)	1.870(3)	2.216(2)	1.9(1)
$\delta_1 t_1$ (Å)	*27.8(2)*	*20.14(4)*	*26.19(3)*	*20(2)*
σ_2 (Å)	6.652(9)	3.25(3)	5.121(4)	5.9(5)
t_2 (Å)	2.01(1)	4.38(1)	8.46(1)	6.5(7)
$10^6\delta_2$	1.054(7)	2.799(5)	6.517(2)	6.1(6)
$\delta_2 t_2$ (Å)	*2.12(2)*	*12.26(4)*	*55.13(7)*	*40(6)*
σ_3 (Å)	4.73(2)	7.505(5)	2.77(2)	4.1(5)
t_3 (Å)	8.07(3)	10.24(2)	11.62(9)	11.2(5)
$10^6\delta_3$	7.807(4)	7.892(3)	7.341(2)	7.40(6)
$\delta_3 t_3$ (Å)	*63.0(2)*	*80.81(8)*	*85.3(7)*	*82.61(5)*
σ_4 (Å)	1.80(4)	2.79(2)	2.6(1)	2.1(3)
$\Sigma_{i=1}^{2} t_i$ (Å)	*17.53(1)*	*15.15(1)*	*20.28(1)*	*17.0(7)*
$\Sigma_{i=1}^{3} t_i$ (Å)	*25.60(3)*	*25.39(2)*	*31.9(1)*	*28.1(8)*
$\Sigma_{i=1}^{2} \delta_i t_i$	*29.9(3)*	*32.4(1)*	*81.4(7)*	*55(4)*
area per molecule (Å^2)	*55.6(6)*	*51.3(2)*	*20.5(2)*	*36(5)*
χ_ν^2	0.64	0.60	0.65	

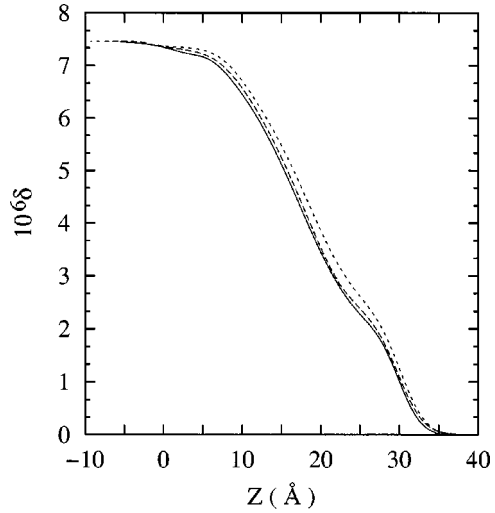

FIG. 5. The contrast variable, $\delta(z)$, obtained from three fits to the data of Fig. 4. Parameters are shown in Table I.

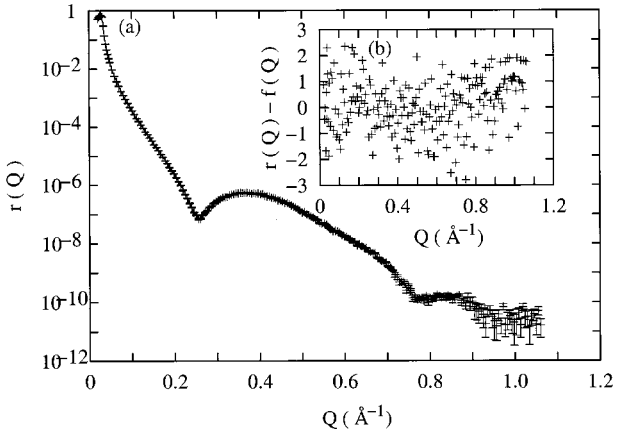

FIG. 6. Simulated data for an SDS layer on a silicon substrate. The solid line is one of five statistically equivalent good fits. The inset shows a plot of the residuals as defined in Eq. (7). Parameters for the five fits are shown in Table II.

density of layer 2 is substantially greater than that of layer 1, as indicated by the parameter, δ. For the SDS molecule this suggests a configuration with head groups downward toward the substrate and tail groups upward. The thickness of the layer 2 in fit *C*, while less than that of the outer region, is substantially larger than the size of the sulfate head group (about 3.5 Å) of the SDS molecule. This suggests a high degree of disorder in the head group region. The product of t and δ, summed over the surfactant regions, is inversely related to the projected area per molecule. For fit *C* this yields 20.5 Å^2, which falls midway between the minimum for close-packed hydrocarbon chains and the L_β (gel) phase. The electron density of the outermost region is considerably lower than either of these two. The complete picture provided by fit *C* is consistent with a layer of SDS molecules which are highly staggered in the direction normal to the surface, with tail groups in nearly the all *trans* configuration. By contrast, fit *B* has an area per molecule of over 50 Å^2, which is considerably greater than required for the liquidlike phase of hydrocarbon chains dominated by *gauche* bonds. Fit *B* also has higher density in layer 2, but the difference is much less than in fit *C*. This could suggest a highly disordered monolayer, having some of the head groups downward, but with substantial intermixing of head and tail groups. The area per molecule of fit *A* is comparable to fit *B*, but in this case it is the outer region which has somewhat higher electron density. This would also suggest a highly disordered monolayer, but with more of the head groups in the upper region.

Obviously, the χ^2 hypersurface for this set of data has multiple minima, at least three of which correspond to excellent but quite distinct fits. On the basis of this analysis, we cannot draw conclusions regarding key structural characteristics: e.g., division of the surfactant layer into separate tail and head regions, the *trans/gauche* isomerization of the tail, or the packing density of molecules on the surface. In the next section, we present an analysis of simulated data in order to explore the conditions which give rise to the observed ambiguity and a resolution of that ambiguity.

B. Analysis of simulated data

We use SPEEDO to generate reflectivity data points which would arise from the x-ray reflection experiment on a plausible SDS monolayer. To these data we add random numbers, Gaussian distributed about zero, scaled proportionally to the squareroot of the reflectivity. To mimic experimental data in which statistical accuracy worsens as the reflectivity decays (in spite of adjustments in counting time and source power), different proportionality factors are used in different sections of the simulated data. The magnitude of the added noise is comparable to that for the experimental data in Fig. 4.

In our simulations, we exclude limitations on Q due to diffuse scattering. Thus the simulated data (Fig. 6) cover an even larger range of Q and reflectivity than our real data (Fig. 4). Further, the SPEEDO algorithm generates data similar to but not identical to real experimental data. Approximate correction factors (e.g., overfilling of the sample by the incident beam and scaling of the data to unit reflectivity) used in analyzing real data are simulated as if they were exact. Since we will show below that simulated data give rise to the same difficulty of interpretation as seen in real data, it is clear that neither instrumental complications nor limits on Q due to diffuse scattering can be the sole cause of ambiguity.

The simulated data shown in Fig. 6 are generated from a model in which the tail groups are in the L_α (liquidlike) state and the electron density in the head region is determined by stoichiometry. The complete set of model parameters is shown in Table II. Following the procedure of the preceding section, we performed eighteen simulated annealings and found five distinctly different, good fits to the data, all of which are statistically indistinguishable. One of these fits is shown in Fig. 6. Parameters for the five distinct, good fits are shown in Table II. Figure 7 shows that dramatically different density profiles can fit the same data set. The trends across these fits are virtually identical to those for the experimental data: The results of the individual fits do not agree with the parameters used to generate the data. Further, equally valid fits give very different pictures of the monolayer.

The ensemble of fits to the simulated data is consistent with a χ^2 hypersurface as illustrated in Fig. 3(b). Instead of a

TABLE II. Five acceptable fits to simulated data for an SDS monolayer and comparison to the model parameters. Standard errors on individual fitting parameters are omitted for clarity. The ''Average'' column contains the unweighted mean of parameters for these five fits (standard deviation in parentheses). Quantities in italics are derived from the fitting parameters.

Parameter	Fit *A*	Fit *B*	Fit *C*	Fit *D*	Fit *E*	Average	Model
σ_1 (Å)	3.219	2.465	2.713	2.248	2.859	2.7(3)	**2.40**
t_1 (Å)	1.721	12.67	11.74	12.66	10.42	10(4)	**11.5**
$10^6\delta_1$	2.727	3.428	3.013	2.616	3.425	3.0(3)	**2.85**
$\delta_1 t_1$ (Å)	*4.69*	*43.4*	*35.4*	*33.1*	35.7	*30(13)*	**32.7**
σ_2 (Å)	2.206	3.408	2.311	3.408	7.251	4(2)	**2.40**
t_2 (Å)	11.48	6.524	2.315	6.435	2.011	6(3)	**3.60**
$10^6\delta_2$	3.971	7.241	5.281	7.221	1.581	5(2)	**5.55**
$\delta_2 t_2$ (Å)	*45.6*	*47.2*	*12.2*	*46.5*	*3.18*	*31(19)*	**19.9**
σ_3 (Å)	2.603	8.999	2.856	8.661	3.232	5(3)	**2.40**
t_3 (Å)	17.09	10.00	15.10	10.01	16.57	14(3)	**14.0**
$10^6\delta_3$	7.201	7.109	7.073	6.983	7.082	7.09(7)	**7.05**
$\delta_3 t_3$ (Å)	*123.1*	*70.1*	*106.8*	*69.9*	*117.3*	*97(23)*	**98.7**
σ_4 (Å)	1.686	2.403	2.046	2.641	2.052	2.2(3)	**2.40**
$\Sigma_{i=1}^{2} t_i$ (Å)	*13.2*	*19.19*	*14.05*	*19.10*	*12.43*	16(3)	**15.1**
$\Sigma_{i=1}^{3} t_i$ (Å)	*30.29*	*29.19*	*29.15*	*29.11*	*29.00*	29.3(5)	**29.1**
$\Sigma_{i=1}^{2} \delta_i t_i$	*50.59*	*90.6*	*47.6*	*79.9*	*38.88*	*61(10)*	**52.6**
area per molecule (Å^2)	*33.09*	*18.3*	*34.95*	*20.9*	*42.8*	*30(5)*	**31.5**
χ^2	1.09	1.02	0.965	1.143	1.008		

single, well-defined global minimum, corresponding to the best fit, there are several local minima within e_{χ^2} of one another, all of which represent good fits to the data. The broad minimum in which these local minima occur has a width comparable to the standard deviation obtained by averaging parameters over the set of local minima. By comparing the last two columns of Table II, we can see that the averaged parameters from the ensemble of acceptable fits (next-to-last column in Table II) are all within a standard deviation of the known model parameters.

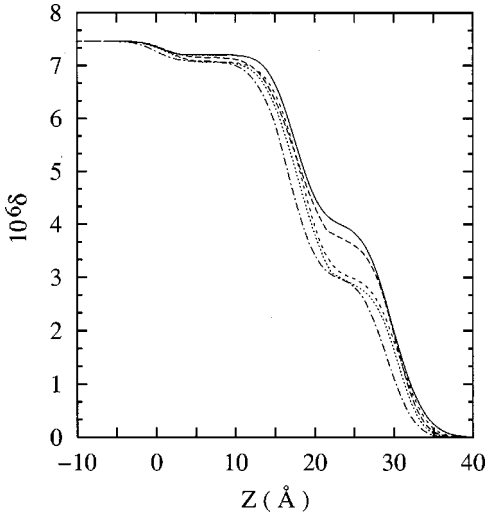

FIG. 7. The contrast variable, $\delta(z)$, obtained from five fits to the simulated data for an SDS monolayer with L_α tails (Fig. 6). The original model is indicated by the solid line. Parameters are shown in Table II.

We conclude that this procedure produces a valid method of arriving at a unique model of the monolayer structure. While each individual good fit describes a monolayer structure consistent with the data, the statistical ensemble of these good fits yields valid estimates for the model parameters as well as their uncertainties. Thus, this analysis of the reflectivity data produces a unique picture of the structure of the monolayer which is highly likely to be correct.

C. Experimental data revisited

Given the procedure suggested by our simulations, we now return to the experimental data for SDS which we examined in Sec. III A. We perform an *additional* thirty-four simulated annealings. Twenty-one fits were ''good,'' with statistically equivalent values of χ^2. The ensemble averaged values of the fitting parameters for these fits (listed in the last column of Table I) yield a picture of the monolayer which has a region of higher electron density (layer 2) adjacent to the substrate. The density suggests SDS head groups with counterions present. The thickness of this region is approximately twice as large as the SDS head group, indicating substantial disorder. The thickness of the outermost (tail group) region and the overall area per molecule are both consistent with hydrocarbon chains in the L_α phase. Thus, the tail region likely contains considerable *gauche* conformations and probably dictates the molecular spacing. The roughness of the outermost interface (between the air and the tail groups) is comparable to the expected 2–4 Å rms roughness which is typical of polished silicon crystals. This shows that the monolayer as a whole follows the contours of the solid surface. The roughness of the interfaces bounding the head group region is two to three times larger than the outermost interface, again consistent with a highly disordered head region. The density of the third region is consistent with the known structure of low-density SiO_2, and the thickness of the layer is typical of native oxide layers on silicon crystals. Thus, by averaging the parameters obtained from an ensemble of statistically equivalent, good fits to the data, we obtain a model which is physically plausible in every detail. The uncertainties in the parameters give reasonably tight bounds on all parameters compared to the benchmark values we discussed in Sec. I.

Since the thickness of the head group region is at the limit of our length scale resolution, conclusions about structural details of this region are rather tenuous. However, the presence of counterions, as suggested by the ensemble averaged fitting parameters, provides insight into the physics of the formation of the SDS monolayer. The organic ion of the SDS molecule has the same charge as the silica substrate at neutral pH. Thus, a self-assembled monolayer is unlikely to form at the solid/liquid interface if the counterion and organic ion are mostly dissociated in solution. With counterions present in the head group region, the organic ion is neutralized, enabling the molecule as a whole to be attracted to the substrate.

IV. IMPROVED COUNTING STATISTICS

The data we examined above had statistics typical of an experiment using a rotating anode source. Given the avail-

ability of synchrotron sources, we ask what changes in the situation described above will occur if these more powerful sources were used. First, the issue of sample degradation must be treated carefully since high x-ray doses are known to degrade surfactant monolayers [12]. Second, since the separation of the signal at high Q into specular and diffuse components depends on the instrumental resolution, the higher resolution available at synchrotron sources, combined with increased flux, may provide an additional decade or more of specular intensity. Depending on the sample, this could extend the Q range of the reflectivity data to approximately 1 $Å^{-1}$. However, as we suggested in the preceding section, limitation of the Q range due to diffuse scattering does not seem to be a significant cause of ambiguity of interpretation. Finally, we could obtain reflectivity data with better statistics at all Q. In this section we investigate the effects of these higher counting statistics.

We use the same simulated SDS model as above, but add scatter to the ideal model data which is reduced by a factor of 10. In a real measurement, this would correspond to 100 times the counting statistics. Thirty fits were performed from a variety of initial parameter sets. Three of these fits are ''good'' and locate the same minimum in the χ^2 hypersurface. Further, the parameters obtained at this minimum are within the standard error of the original model parameters. Thus, extremely precise data allow recovery of the correct parameters for even this rather smeared electron density profile (similar to Fig. 7) and the uncertainties in these parameters are decreased by the higher statistics.

A caveat to the above conclusion is that the reduced noise has made the global minimum extremely narrow and difficult to locate [see Fig. 3(c)]. Further, a second best set of parameters exists which is much more easily located than the first (found in eight out of the thirty attempts). Our criteria reject this as a ''good'' fit because the residuals plot contains systematic features. However, if the lower minimum were missed in the statistical survey, one might assume this was the best possible fit and add another layer, unnecessarily overparametrizing the fit. Since the global minimum is so difficult to find, we tried adding additional Gaussian noise to the data. We found that when the noise is comparable to that of the previous SDS simulation (and to our experimental data sets) we could follow the procedure outlined in Sec. III and obtain multiple ''good'' fits. Using each of these fits as starting points for fits to the nondegraded data, we recovered the correct best fit from at least one of these starting points.

V. DISCUSSION AND CONCLUSIONS

Relative contrasts between the subsections of the monolayer can improve or degrade the ability of reflectivity data to discern monolayer structure. We have discussed in detail experimental data and simulations for SDS with tail groups in the L_α (liquidlike) state. Even with signal-to-noise data typical of a rotating anode experiment, most of the important physics of the monolayer structure can be deduced by ensemble averaging of the fitting parameters for all statistically equivalent good fits. High signal-to-noise data are required to discern the details of the head group region. We attribute this to the relatively poor electron density contrast between the SDS head group and the underlying SiO_2 layer. To examine

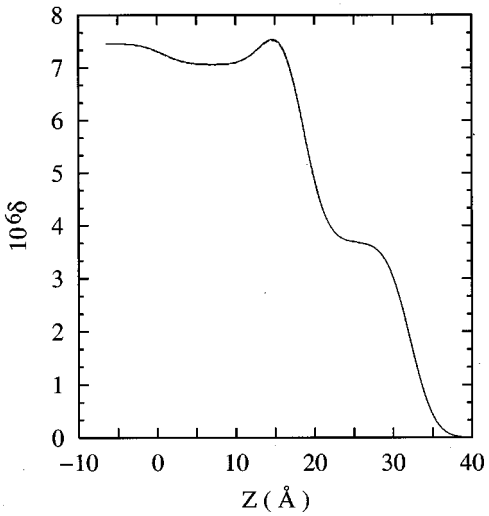

FIG. 8. The contrast variable, δ, for a simulated SDS monolayer with L_β tails. The solid line is the model. The dashed line is a fit to the data with added noise.

cases where contrasts are greater, we have also performed simulations for monolayers of cetyl trimethylamonium bromide ($C_{16}TAB$) with tail groups in the L_α state, and for SDS with tails in the L_β (gel-like) state. For $C_{16}TAB$ the electron density contrast is good between head group and substrate, but poor between the head and tail regions. Like L_α SDS, the monolayer has a region which is not well resolved as a separate layer, and the results of fitting the data are similar. At lower signal-to-noise ratio, the essential physics of the monolayer is recoverable, but there is a high degree of uncertainty in the details of the head group region. At higher signal-to-noise ratio all of the structural details are recovered. For L_β SDS, the electron density of the head group is significantly higher than that of the underlying SiO_2. As can be seen in Fig. 8, the head group region is better resolved as a separate layer. All of the structural details of this monolayer were recovered by ensemble averaging of the good fits, even for lower signal-to-noise data.

A possible concern when using high statistics data is that the measurement becomes highly sensitive to the functional form of the interfacial density profiles. The error function profile, which is the typical form used to fit data, may not be correct and may give misleading information. To test this idea, we simulated a data set in which the profile connecting the head and tail regions of the molecule follows a hyperbolic tangent form. We fitted this data set in the usual way, assuming error-function transitions at all interfaces. The result is essentially a null result: the error function fits the hyperbolic tangent to within a few percent; there is very little difference between these functional forms.

We have outlined a procedure for analyzing reflectivity data that yields reliable and objective structural information for monolayer systems. The χ^2 hypersurface is probed by performing multiple fits to the data from a variety of starting points using the method of simulated annealing. For a monolayer system in which the features are not all well resolved and the signal-to-noise ratio is comparatively low, multiple statistically equivalent minima exist in the χ^2 hypersurface which correspond to different physically plausible structural

pictures. For this reason, a single good fit to the data is insufficient to make certain types of claims of structural detail. The interpretation of the data must be derived from the average and standard deviation of fitting parameters across an ensemble of statistically equivalent, good fits. Since the global minimum in the χ^2 hypersurface may be too sharp to locate in a reasonable amount of computing time for high signal-to-noise data, it may be difficult to find any good fit. One can try the addition of noise as an intermediate step. An appropriate amount of noise will broaden the χ^2 minimum. If good fits are found, the corresponding parameters for at least one of them should be within a standard error of the correct ones. One can then remove the added noise and start a fit with each of the previously obtained parameter sets to see if a good fit is obtained.

Whereas genetic algorithms may provide an efficient way to eliminate all but the best possible fit to the data, our simulations indicate a need to perform multiple fits in order to get a sense of the complexity of the χ^2 hypersurface. There may exist parameter sets which are different from the correct model, but which yield equally ''good'' or slightly ''better'' fits to the data. Thus, reliance on only a single good fit—even the best possible fit—may be misleading. Our results suggest that neither uncertainty in instrument parameters nor limitations on the range of Q due to diffuse scattering are significant causes of this ambiguity. Rather, the apparent ambiguity in the monolayer structure is the result of inadequate surveying of the χ^2 hypersurface, particularly when there is poor contrast in the electron density profile and/or insufficient signal-to-noise ratio.

Although we have focused in this paper on the structure of surfactant monolayers, our method can be generalized to any monolayer system, including thiols, block copolymers, etc. Our results have shown that high signal-to-noise data are not necessarily required to deduce all of the structural details of a monolayer, provided that the various regions of the sample are well resolved in the electron density profile. Unfortunately, this is often not the case. The success of neutron reflectivity depends upon isotopic substitution to compensate for the comparatively low source intensity. But there is no analogous technique for x rays. Perhaps the most important conclusion of our work is that the essential physics of monolayer structures can still be deduced—even when the electron density contrast is not high for all the regions—by thoroughly surveying the χ^2 hypersurface and ensemble averaging the parameters obtained from all statistically equivalent good fits.

ACKNOWLEDGMENT

This material is based upon work supported by the National Science Foundation under Grant No. DMR9802290.

APPENDIX: SPEEDO

Our computer program, called SPEEDO [32], uses a dynamically optimized Monte Carlo [26] simulated annealing [27] technique to find optimal parameter sets. The use of such a complex algorithm is justified when the χ^2 hypersurface, defined in the space of fitting parameters, is rough and has more than one local minimum. Here, we briefly describe simulated annealing and our implementation of the dynamic optimization technique.

In applying simulated annealing to least-squares fitting, χ^2 takes the role of an energy function, and Boltzmann statistics with an effective temperature, T, are applied to trial changes in parameters (or ''moves''). The analogy is to thermal annealing and slow cooling of a physical system in order to put the system into its ground state. Trial moves are generated through a random process (see below). A move which reduces χ^2 is always accepted (i.e., the fitting parameters are updated to the trial set). A move which increases χ^2 is accepted with probability $e^{-\Delta\chi^2/T}$. In our algorithm, the number of Monte Carlo trial moves at each T is adjustable, and is scaled by a factor $d^{2.5}$, where d is the number of free parameters in the fit. Thus, as the dimensionality of the parameter set becomes large, simulations become time consuming. As the simulation proceeds, T is reduced in an attempt to find the global minimum of χ^2 and the corresponding parameter set. In our algorithm, T is reduced exponentially, with an adjustable number of steps per decade. A typical simulated annealing used in this paper performs 6324 trial moves at each temperature, with four temperature steps per decade.

We have implemented the dynamic optimization procedure of Bouzida, Kumar, and Swendsen [26]. This procedure adjusts the average step size in any direction in the parameter space so that the acceptance ratio for trial moves is neither too large nor too small. Small steps lead to slow changes in χ^2 even if all trials are accepted; large moves lead to slow changes in χ^2 because few trials are accepted. During the simulation, the size and shape of a d-dimensional correlation ellipsoid is adjusted; each trial move is then defined in a random direction in this ellipse, with larger changes in ''soft'' directions than in ''hard'' directions.

We mention here a few of the details of how SPEEDO works. The program can either generate a reflectivity curve based on input parameters (''forward model'') or it can read a data file and perform a fit. The reflectivity can be calculated in several ways. The computationally efficient ''$Q-Q_t$'' approximation [24,29] is appropriate when all layers are thicker than their bounding roughnesses. The rigorous optical calculation [28,23] is more general. The program inserts error-function transitions between layers with widths given by the roughness parameters. The error function is approximated by a series of steps of width $\pi/(8Q_{\max})$. One may also read a file with an arbitrary δ vs z and have SPEEDO generate the corresponding reflectivity. There are several instrument parameters. The reciprocal space resolution is computed from the angular divergence of the input beam. The program checks the spacing of experimental data points and gives a warning if this spacing is larger than the resolution. In this case, a file is generated which contains the original data points plus additional points (with 100% errors) which facilitate correct computation of the resolution convolution sum. A wavelength distribution can also be included (convenient for neutron work). A correction is made to the computed reflectivity for the case where a fraction of the input beam misses the sample at low angle ($\sim \sin\alpha/\sin\alpha_b$ as long as this is <1, α_b being the minimum angle at which the complete width of the beam is on the sample) [13]. Finally, an overall normalization factor multiplies the computed curve. It should be noted that in fitting, these instrument

parameters can interact with the physical parameters describing layer structures. While the instrument parameters can be used as fitting parameters, one must determine the values as closely as possible through independent measurements (see main text).

All parameters describing a layer structure and all the instrument parameters are potential fitting parameters. Each potential parameter is given an initial value which (i) can be fixed, (ii) can be constrained to a specified range, or (iii) can be tied to a similar parameter in another layer (convenient for multilayer samples). Narrowing the variation of a parameter to a physically plausible range reduces the volume of parameter space which must be covered and makes simulation more efficient. One may specify the composition of a layer by defining a molecular scattering length and absorption cross section (then allowing the molecular number density to vary), or one can describe a layer by independent variation of δ and β. The incident medium can be defined to be other than vacuum and can be included in the fitting parameters (again convenient for neutron work and for electrochemical studies [33]).

In contrast to standard χ^2 minimization algorithms [31], simulated annealing allows the parameter set to move over local maxima to locate deep minima far from the starting point. For a rough χ^2 surface, however, performance of simulations and interpretation of results is not straightforward. We demonstrate in the body of this paper a means of dealing with such complex situations.

[1] S. Garoff, Thin Solid Films **152**, 49 (1987).

[2] J. D. Swalen, D. L. Allara, J. D. Andrade, E. A. Chandross, S. Garoff, J. Israelachvili, T. J. McCarthy, R. Murray, R. F. Pease, J. F. Rabolt, K. J. Wynne, and H. Yu, Langmuir **3**, 932 (1987).

[3] S. A. Safran, M. O. Robbins, and S. Garoff, Phys. Rev. A **33**, 2186 (1986).

[4] B. M. Ocko, X. Z. Wu, E. B. Sirota, S. K. Sinha, O. Gang, and M. Deutsch, Phys. Rev. E **55**, 3164 (1987).

[5] W. J. Sun, S. Tristram-Nagle, R. M. Suter, and J. F. Nagle, Biophys. J. **71**, 885 (1996).

[6] J. F. Nagle, R. Zhang, S. Tristram-Nagle, W. J. Sun, H. I. Petrache, and R. M. Suter, Biophys. J. **70**, 1419 (1996).

[7] T. J. McIntosh and S. A. Simon, Biochemistry **25**, 4948 (1986).

[8] A. Ulman, *An Introduction to Ultrathin Organic Films* (Academic Press, San Diego, 1991), p. 283ff.

[9] R. K. Heilmann and R. M. Suter, Phys. Rev. B **59**, 3075 (1999).

[10] J. Shindler and R. M. Suter, Rev. Sci. Instrum. **63**, 5343 (1992).

[11] I. M. Tidswell, B. M. Ocko, P. S. Pershan, S. R. Wasserman, G. M. Whitesides, and J. D. Axe, Phys. Rev. B **41**, 1111 (1990).

[12] A. Malik, W. Lin, M. K. Durbin, T. J. Marks, and P. Dutta, J. Chem. Phys. **107**, 645 (1997).

[13] A. Gibaud, G. Vignand, and S. K. Sinha, Acta Crystallogr., Sect. A: Found. Crystallogr. **49**, 642 (1993).

[14] W. R. Birch, M. A. Knewtson, S. Garoff, and R. M. Suter, Langmuir **11**, 48 (1995).

[15] P. N. Thirtle, Z. X. Li, R. K. Thomas, A. R. Rennie, S. Satija, and L. P. Sung, Langmuir **13**, 5451 (1997).

[16] W. R. Birch, M. A. Knewtson, S. Garoff, R. M. Suter, and S. Satija, Colloids Surface **89**, 145 (1994).

[17] J. R. Lu, E. M. Lee, and R. K. Thomas, Acta Crystallogr., Sect. A: Found. Crystallogr. **52**, 11 (1996).

[18] A. Asmussen and H. Riegler, J. Chem. Phys. **104**, 8159 (1996).

[19] A. D. Dane, A. Veldhuis, D. K. G. de Boer, A. J. G. Leenaers, and L. M. C. Buydens, Physica B **253**, 254 (1998).

[20] J. R. Lu and R. K. Thomas, Nucl. Instrum. Methods Phys. Res. A **354**, 149 (1995).

[21] P. S. Pershan, Phys. Rev. E **50**, 2369 (1994).

[22] B. Frank and S. Garoff, Colloids Surface **116**, 31 (1996).

[23] J. H. Underwood and T. W. Barbee, Jr., in *Low Energy X-ray Diagnostics*, edited by D. T. Atwood and B. L. Henke, AIP Conf. Proc. No. 75 (AIP, New York, 1981).

[24] S. K. Sinha, E. B. Sirota, S. Garoff, and H. B. Stanley, Phys. Rev. B **38**, 2297 (1988).

[25] D. Bouzida, S. Kumar, and R. H. Swendsen, Phys. Rev. A **45**, 8894 (1992).

[26] A. M. Ferrenberg and R. H. Swendsen, Phys. Rev. Lett. **63**, 1195 (1989).

[27] S. Kirkpatrick, J. Stat. Phys. **34**, 975 (1984).

[28] M. Born and E. Wolf, *Principles of Optics*, 4th ed. (Pergamon Press, Oxford, 1970), p. 55ff.

[29] L. Nevot and P. Croce, Rev. Phys. Appl. **15**, 761 (1980).

[30] P. R. Bevington and D. K. Robinson, *Data Reduction and Error Analysis for the Physical Sciences*, 2nd ed. (McGraw Hill, New York, 1992), p. 212ff.

[31] P. R. Bevington and D. K. Robinson, *Data Reduction and Error Analysis for the Physical Sciences* (Ref. [30]), p. 68.

[32] This program was written by M. Knewtson and R. M. Suter and is available by anonymous FTP in the form of a self-extracting file, `inspeed.exe`, located on `x2d.phys.cmu.edu` in the `pub` directory. Executing this file on a Windows machine will generate an executable, source code, and a documentation file with usage hints. Comments and suggestions should be sent to R.M.S. at suter@andrew.cmu.edu.

[33] J. Wang, B. M. Ocko, A. J. Davenport, and H. S. Isaacs, Phys. Rev. B **46**, 1032 (1992).